scientific reports

Check for updates

OPEN

Ni–Fe phosphide deposited carbon felt as free-standing bifunctional catalyst electrode for urea electrolysis

Woo Hyun Yun[1,5], Gautam Das[2,5], Bohyeon Kim[1], Bang Ju Park[3], Hyon Hee Yoon[1]✉ & Young Soo Yoon[4]✉

A free-standing catalyst electrode for the urea oxidation reaction (UOR) and hydrogen evolution reaction (HER) in a urea electrolysis cell was synthesized by electroplating a Ni–Fe alloy onto carbon felt, followed by phosphidation (P-NiFe@CF). The prepared P-NiFe@CF catalyst consisted of Ni_5P_4, NiP_2, and FeP with 3D flower-like P-NiFe architecture on CF. P-NiFe@CF exhibited excellent electrocatalytic activity for the UOR (demanding only 1.39 V (*vs.* RHE) to achieve 200 mA cm^{-2}), and for the HER with a low overpotential of 0.023 V (*vs.* RHE) at 10 mA cm^{-2}, indicating its feasibility as a bifunctional catalyst electrode for urea electrolysis. A urea electrolysis cell with P-NiFe@CF as both the free-standing anode and cathode generated a current density of 10 mA cm^{-2} at a cell potential of 1.37 V (*vs.* RHE), which is considerably lower than that of water electrolysis, and also lower than previously reported values. The results indicate that the P-NiFe@CF catalyst electrodes can be used as free-standing bifunctional electrodes for urea electrolyzers.

Hydrogen (H_2) has recently gained significant attention as a clean energy source because of its high calorific value and environmental friendliness relative to other hydrocarbon-based fuels. Unlike methane reforming, hydrogen production from water splitting is carbon–neutral and is an inexpensive process that generates high purity H_2[1]. However, the sluggish oxygen evolution reaction (OER) impedes the overall efficacy of the water-splitting reaction. Thus, to overcome the high overpotential of the OER, readily oxidizable species, such as hydrazine, ethanol, and urea have been explored for reducing the overpotential[2]. In particularly, hydrogen production from urea is of interest because urea is non-flammable, non-toxic, and low-cost, and the denitrification of urea-rich wastewater can be achieved with the simultaneous production of H_2[3–5]. The theoretical potential for water electrolysis is 1.23 V, whereas that for urea electrolysis is as low as 0.37 V; however, the actual electrolysis cell voltages for water and urea are still high[6]. The high overpotential of urea electrolysis is due to the fact that the anodic urea oxidation reaction (UOR) is a complex process that involves $6e^-$ transfers resulting in sluggish kinetics[7–9]. The sluggish kinetics of the UOR remains a challenge for the practical implementation of urea electrolysis. Against this backdrop, a high-performance bifunctional catalytic system for the anodic UOR and cathodic hydrogen evolution reaction (HER) to facilitate urea electrolysis for H_2 production has been demanded.

Although, noble metal catalysts such as Pt/C, RuO_2, and IrO_2 are usually preferred for urea electrolysis, their high cost and scarcity limit their large-scale use. Recently, Ni-based materials have been studied as bifunctional UOR and HER catalysts as alternatives to noble group metals[5,9–12]. The Ni-catalyzed UOR suffers from the disadvantages of a large overpotential and susceptibility of the catalysts to CO poisoning. Yan et al.[7] reported that the overpotential of urea electrolysis could be reduced by the incorporating Co or Zn into the Ni structure. Singh et al.[13] showed that Sn in NiSn facilitated OH^- adsorption on NiSn, resulting in stable UOR peak current densities. Yu et al.[14] reported that Ni–Mo–O nanorod-derived composited catalysts afforded a reduced overpotential and a smaller Tafel slope (i.e. 19 mV) for the UOR, with long-term stability. Several other Ni-based catalysts have been reported, such as $Ni(OH)_2$[15], Ni_2P/Fe_2P[1], Ni nanosheets[16], Ni_3S_2 on Ni foam[17], NiFeCo[18], and $LaNiO_3$[19], with

[1]Department of Chemical and Biological Engineering, Gachon University, Seongnam, Gyeonggi-do 461-701, Republic of Korea. [2]Department of Polymer Science and Engineering, Kyungpook National University, Sangyeok-dong, Buk-gu, Daegu, Korea. [3]Department of Electronic Engineering, Gachon University, Seongnam, Gyeonggi-do 461-701, Republic of Korea. [4]Department of Materials Science and Engineering, Gachon University, Seongnam, Gyeonggi-do 461-701, Republic of Korea. [5]These authors contributed equally: Woo Hyun Yun and Gautam Das. ✉email: hhyoon@gachon.ac.kr; benedicto@gachon.ac.kr

Samples	Chemicals	Composition ($g\ L^{-1}$)
Ni@CF	$NiSO_4{\cdot}7H_2O$	200
	$NiCl_2{\cdot}6H_2O$	40
	H_3BO_3	60
	$Na_3C_6H_5O_7$	79
NiFe@CF	$NiSO_4{\cdot}7H_2O$	200
	$NiCl_2{\cdot}6H_2O$	40
	H_3BO_3	60
	$Na_3C_6H_5O_7$	79
	$FeCl_2{\cdot}6H_2O$	40

Table 1. Composition of different baths used for deposition.

good catalytic performance. However, designing bifunctional catalysts that exhibit excellent activity for both the UOR and HER still remains a challenge.

Ni–Fe alloys have shown great potential for water splitting under alkaline conditions[20,21]. It has been reported that Fe in Ni promotes the formation of more conducting NiOOH, which can dramatically enhance the reaction rates[22–25]. In addition, Fe–Ni based oxides[26], metal–organic frameworks[27], phosphides[28], nitrides[29,30], and chalcogenides[32] have been evaluated for the OER and HER. These catalysts demonstrated excellent OER activities; however, their overall efficiency still remains low owing to the poor HER performance (requiring over 1.65 V *vs.* RHE to drive a current density of 10 mA cm^{-2}). Among the various metal catalysts, phosphides have emerged as competent candidates for the HER in alkaline electrolytes[33]. The negatively charged phosphorous atom in metal phosphides can effectively trap protons during the electrochemical HER process[34]. Furthermore, metal phosphides have good stability over a wide pH range. Recent studies have shown that bimetallic phosphides are attractive choices compared to monometallic phosphides because the incorporation of a second metal modulates the electronic structure[35]. For example, Husam et al. reported NiCoP as a superior bifunctional catalyst for the HER and OER in alkaline media[36]. Several bimetallic phosphides, such as MnNiP, AgCoP, FeNiP, and NiCoP have been reported as efficient bifunctional catalysts[37–46]. While a few studies on monometallic Ni phosphides have been reported[47,48], there are limited studies on bimetallic phosphides for simultaneous UOR and HER. This may be due to the difficulties that arise from the complicated and uneconomical process of integrating the merits of UOR and HER activity in single bifunctional catalysts for both reactions in the same electrolyte. Commonly, the catalytic process occurs on metal surfaces. In case of powdered materials, the exposed active surface area is relatively low, and the electron/ion transport is limited. Therefore, suitable conducting support materials should be selected for the rational design of efficient electrodes. Most support materials have three-dimensional (3D) structures as support material can offer highly exposed active sites, better permeation of electrolytes, and good electron transport. Recently, the direct growth of metal catalysts on support materials has been widely explored[49–53]. These types of electrodes maintain a high surface area and porous network structure, which are conducive for efficient electron transport, thus enhancing the conductivity.

Thus, in this study, we report a highly scalable and convenient approach for fabricating self-supporting carbon electrodes (e.g., carbon felt) with incorporated P-NiFe as bifunctional electrocatalysts for the UOR and HER. The support is decorated with the metal catalysts by electroplating, followed by phosphorization in phosphorus vapor. This study demonstrates that Ni–Fe bimetal phosphide-decorated carbon felt can be directly used as a bifunctional catalyst electrode with excellent catalytic activity and good stability in urea electrolysis cells.

Methods

Materials and synthesis of catalyst electrodes. As obtained carbon felt (CF; Carbon Fiber Co., China) was heated at 1000 °C for 2 h at a rate of 2.5 °C/min under continuous nitrogen purging to remove organic impurities. Afterward, the CF was treated with an acid solution (H_2SO_4:HNO_3:H_2O in a ratio of 1:1:1) for 24 h at 60 °C. The acid-treated CF was then washed with ethanol and acetone and dried in a vacuum oven overnight at 45 °C. Following the acid treatment, the CF (2.0 × 4.0 cm) was attached to a platinum wire and used as the working electrode, whereas Ni foam was used as the counter electrode. The CF electrode and counter electrode were immersed in the electroplating solutions (Table 1), where the distance between the electrodes was maintained at 1 cm. The electroplating solution was purged with nitrogen for 20 min, after which electrodeposition was carried out using a DC power supply by applying a constant current of 70 mA cm^{-2} for 1 h at 60 °C. The obtained Ni- or Ni–Fe-deposited CF (denoted as Ni@CF or NiFe@CF) was washed with water, and then dried in a vacuum oven.

The phosphidation of NiFe@CF was then carried out under phosphorus vapor; in which, 1 g of red phosphorus was placed upstream of a porcelain boat, and NiFe@CF (2 × 2 cm) was placed 1 cm downstream. Subsequently, phosphidation was carried out in a tube furnace at 550 °C for 2 h at a rate of 2 °C/min under continuous nitrogen flow. The phosphorized sample is denoted as P-NiFe@CF. A whitish-gray material was obtained after phosphidation.

Characterization. The morphological characteristics and structures of the samples were studied using a scanning electron microscope (SEM, JEOL JSM-6700F) equipped with an energy-dispersive X-ray spectroscopy (EDX) and a high-resolution transmission electron microscope (HRTEM, JEOL JEM-4010). The XRD measure-

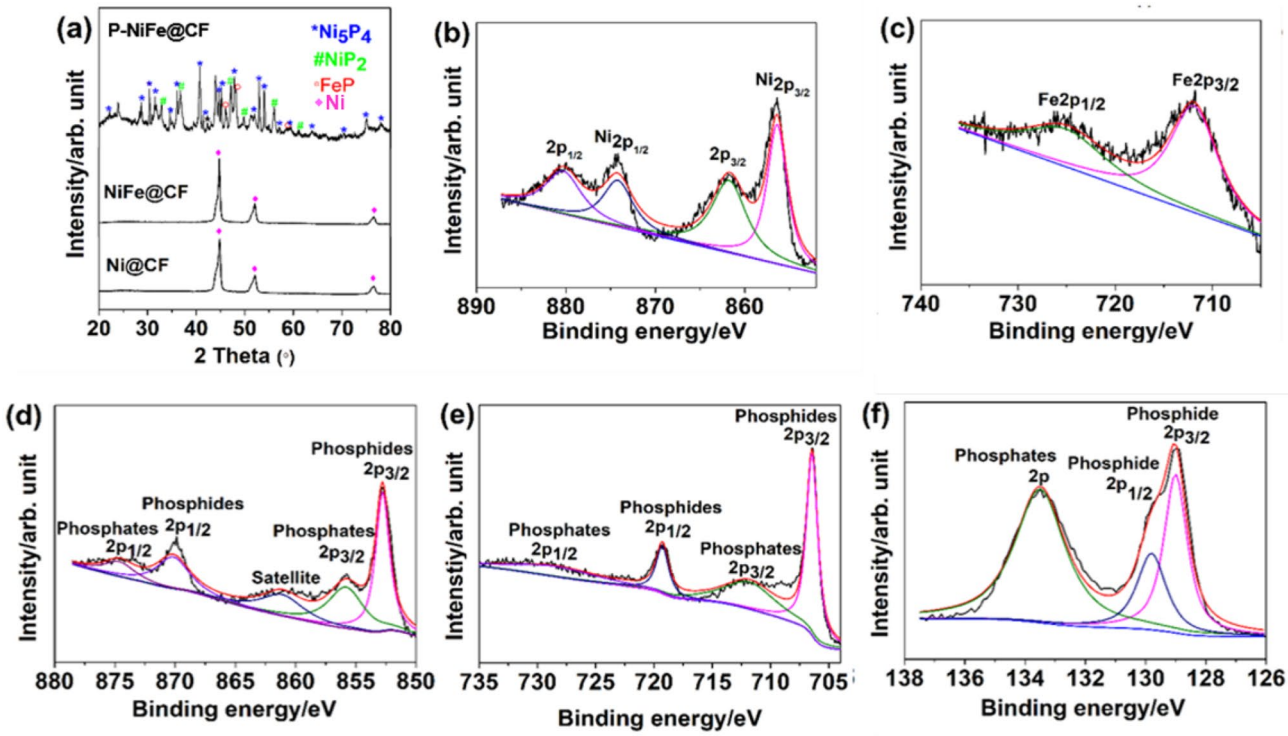

Figure 1. (**a**) XRD patterns of Ni@CF, Ni–Fe@CF, and P-NiFe@CF; and XPS binding energy plots for (**b**) Ni2p and (**c**) Fe2p peaks of Ni–Fe@CF, and Ni2p (**d**), Fe2p (**e**), and P2p (**f**) peaks of P-NiFe@CF.

ments were carried out with a Rigaku X-ray diffractometer with Cu Kα radiation (λ = 1.5418 Å) at a scan rate of 2°/min at an operating voltage of 40 keV and 20 mA. X-ray photoelectron spectroscopy (XPS, K-alpha, Thermo VG, U.K.) employing a monochromated Al X-ray source (Al Kα line: 1486.6 eV) was used to obtain the binding energy plots of the samples.

Electrochemical measurements. The electrochemical activities of the catalyst samples were evaluated by linear sweep voltammetry (LSV), chronoamperometry (CA), and electrochemical impedance spectroscopy (EIS) using a potentiostat–galvanostat (SP-240, Bio-Logic, France). The EIS profiles of the samples were acquired in the frequency range of 100 kHz to 100 μHz. A conventional three-electrode system was used for the electrochemical measurements. The as-prepared freestanding electrode was directly used as the working electrode; and Hg/HgO (1 M NaOH) and a platinum wire were used as reference and counter electrodes, respectively. All LSV plots were obtained in aqueous KOH under ambient conditions at a scan rate of 5 mV s^{-1}. CA measurements of Ni@CF, Ni–Fe@CF, and P-NiFe@CF were performed in 0.33 M urea in 1 M KOH under an applied voltage of 1.43 and − 0.276 V (*vs.* RHE) to evaluate the UOR and HER performances, respectively. The data set was calibrated with respect to the reversible hydrogen electrode (RHE) ($E_{RHE} = E_{Hg/HgO} + 0.098 + 0.059 \times pH$).

Results and discussion

Characterization. The XRD patterns of Ni@CF, NiFe@CF, and P-NiFe@CF are shown in Fig. 1a. Ni@CF and Ni–Fe@CF showed well-defined XRD patterns which can be indexed to the fcc structure of Ni (PDF# 98-005-3809)[5,14]. However, no peaks corresponding to Fe were observed in the XRD pattern of Ni–Fe@CF, indicating the substitution of Fe with Ni having the fcc structure. The existence of Fe in NiFe@CF was confirmed by XPS as shown in Fig. 1b. The XRD pattern of P-NiFe@CF exhibited peaks both for both cubic NiP_2 (PDF#98-002-2221) and hexagonal Ni_5P_4 (PDF#98-010-8462). Additionally, the peaks at 46.20°, 48.23°, and 58.96°, ascribed to orthorhombic FeP, were also observed in the XRD pattern of P-NiFe@CF[49]. These results indicated that the P-NiFe@CF catalyst was successfully phosphodized and consisted of NiP_2, Ni_5P_4, and FeP.

The surface elemental composition and valence state of the NiFe@CF and P-NiFe@CF catalysts were analyzed by XPS. Detailed scans of the Ni2p, Fe2p, and P2p regions are shown in Fig. 1b–f. For Ni–Fe@CF, the Ni2p high-resolution spectra displayed peaks at binding energies of 856.4 and 874.3 eV, which were assigned to the $Ni2p_{3/2}$ and $Ni2p_{1/2}$ states, respectively, indicating the existence of Ni^{2+} and Ni^{3+} ions and thus partial oxidation of Ni at the surface[50]. The satellite peaks corresponding to Ni $2p_{3/2}$ and $2p_{1/2}$ spin–orbit couplings were observed at 861.7 and 880.15 eV, respectively[51]. Additionally, the Fe2p peaks of NiFe@CF (Fig. 1c) located at 712.1 and 725.4 eV were ascribed to Fe $2p_{3/2}$ and $2p_{1/2}$, respectively, indicating the successful incorporation of Fe species into the Ni structure, considering the nonexistence of a crystalline structure including Fe (Fig. 1a). In the case of P-NiFe@CF, peaks were observed at 852.78 and 870.16 eV in the Ni2p (Fig. 1d) region, where these values are close to the binding energy of $Ni^{\delta+}$ in Ni_5P_4 and NiP_2, respectively; the result, therefore, indicated increased metallicity of P-NiFe@CF as compared to NiFe@CF. Additionally, the peaks at 855.82 and 874.62 eV are due

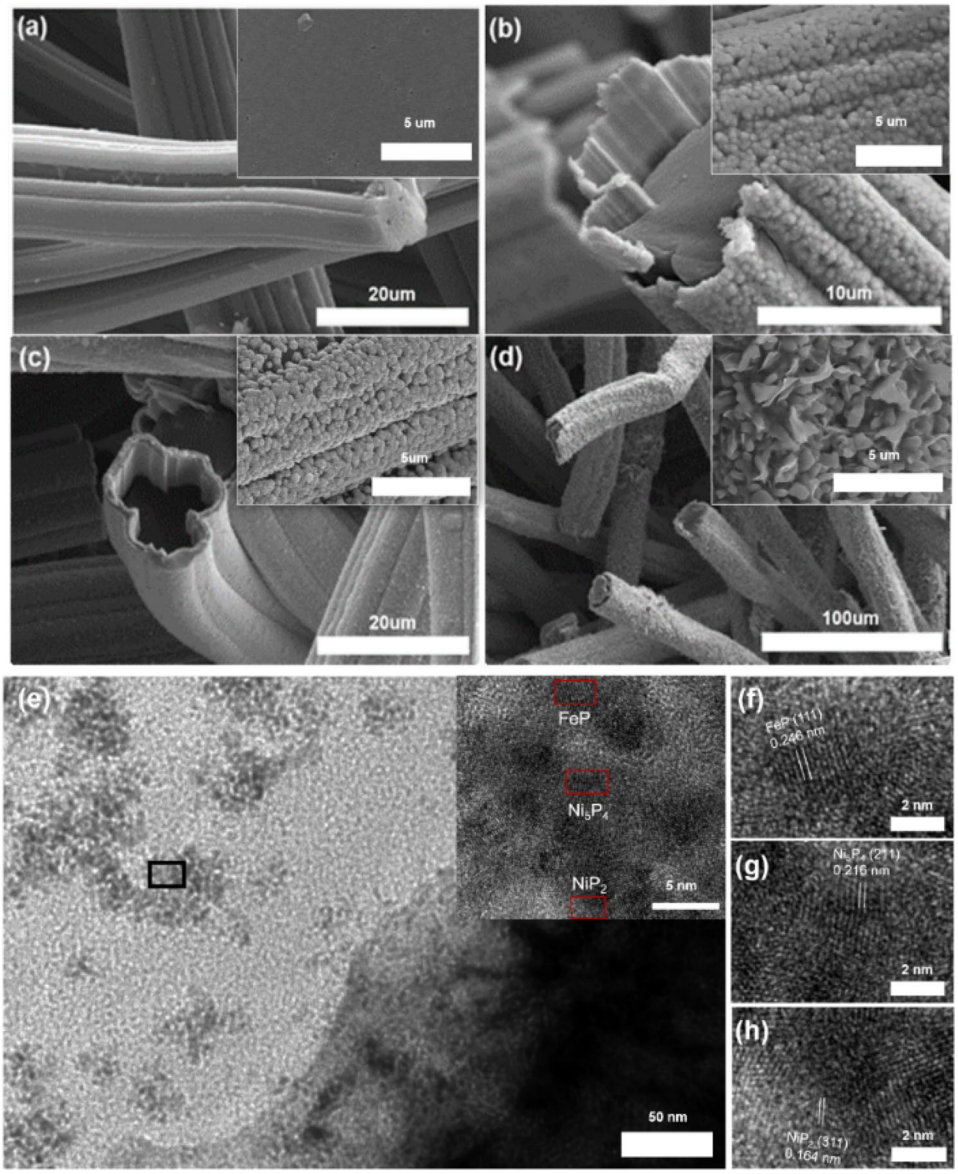

Figure 2. SEM micrographs of (**a**) CF, (**b**) Ni@CF, (**c**) Ni–Fe@CF, and (**d**) P-NiFe@CF with corresponding magnified images; and (**e**–**h**) HRTEM images of P-NiFe@C.

to Ni-PO_x[38,42], while the other peak at 861.13 eV is a satellite peak[42]. The deconvoluted Fe2p spectrum (Fig. 1e) revealed $Fe2p_{3/2}$ peaks at 706.43 and 711.80 eV, derived from Fe–P and Fe–O (corresponding to Fe–P–O_x)[40,42]. Moreover, the peaks at 719.28 and 728.40 eV were assigned to the $Fe2p_{1/2}$ state of Fe–P and Fe–O, respectively[42]. The P2p spectrum displayed two peaks at binding energies of 128.9 and 129.5 eV (Fig. 1f), corresponding to the $2p_{3/2}$ and $2p_{1/2}$ states, respectively, suggesting the existence of a strong bond between $P^{\delta-}$ and the metal[34,36]. The peak at 133.4 eV corresponds to the PO_4^{3-} or P_2O_5 species originating from the oxidation of phosphorus upon exposure to air[40]. Elemental analysis based on XPS results shows the ratio of Ni:Fe:P (15:7:78). The results suggest that the bonds between Ni and Fe were changed to metal-P bonds by phosphorization, forming heterogeneous metal-P mixtures (i.e., Ni_xP_y and FeP). It is obviously reported that phosphide center of the metal phosphide becomes partially negative, making surface of metal positive[50]. Positive metal surface can more easily attract hydroxide ion and make UOR earlier, reducing its overpotential and increasing catalytic performance.

The SEM micrographs of the Ni@CF, Ni–Fe@CF, and P-NiFe@CF samples are shown in Fig. 2. The pristine CF comprised carbon fibers with a diameter of ~ 16 μm, forming an open network 3D structure. As seen in Fig. 2b,c, the individual fibers were completely coated with a thin layer of Ni_xP_y and/or FeP as evidenced by EDX (Suppl. Figs. S1 and S2) and XPS analysis (Fig. 1). The high-resolution image (inset of Fig. 2a–d) revealed a rough surface with granular metal deposits that coalesced to form a continuous thin film. After phosphidation at 550 °C, 3D flower-like P-NiFe architecture on CF was formed as shown in the inset of Fig. 2d. The structure of P-NiFe coated on CF was further characterized by HRTEM, as shown in Fig. 2e–h. The P-NiFe structure comprised Ni_5P_4, NiP_2, and FeP phases, which were identified by their lattice parameters as shown in Fig. 2f–h, in line with

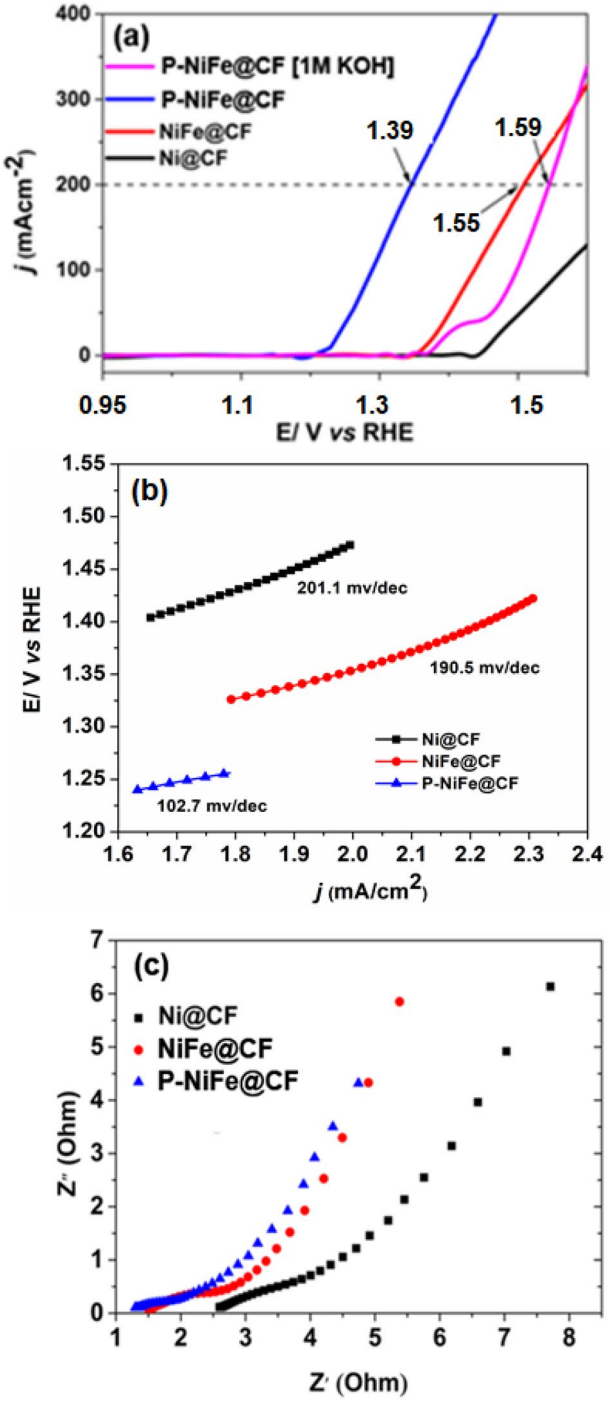

Figure 3. (**a**) LSV curves of Ni@CF, Ni–Fe@CF, and P-NiFe@CF in absence and presence of 0.33 M urea in 1.0 M KOH; (**b**) Tafel plots of different catalyst electrodes; and (**c**) Nyquist plots of different electrodes in 1.0 M KOH.

the XRD analysis. This result suggests intimate contact and strong interactions between the Ni_5P_4, NiP_2, and FeP species in the hybrid structure. Additionally, uniform distribution of Ni, Fe, and P in the P-NiF nanoparticles was observed by TEM elemental EDX mapping (Suppl. Fig. S3).

Electrochemical properties. The electrochemical performances of Ni@CF, Ni–Fe@CF, and P-NiFe@CF catalyst electrodes in the UOR was analyzed by LSV using 1 M KOH and 0.33 M urea at a scan rate of 5 mV s^{-1}, as depicted in Fig. 3. For comparison, bare carbon cloth (CC) and Pt on carbon cloth (Pt@CC) were also analyzed. The oxidation peak at 1.46 V in the LSV plot in 1 M KOH (Fig. 3a) was ascribed to the formation of active

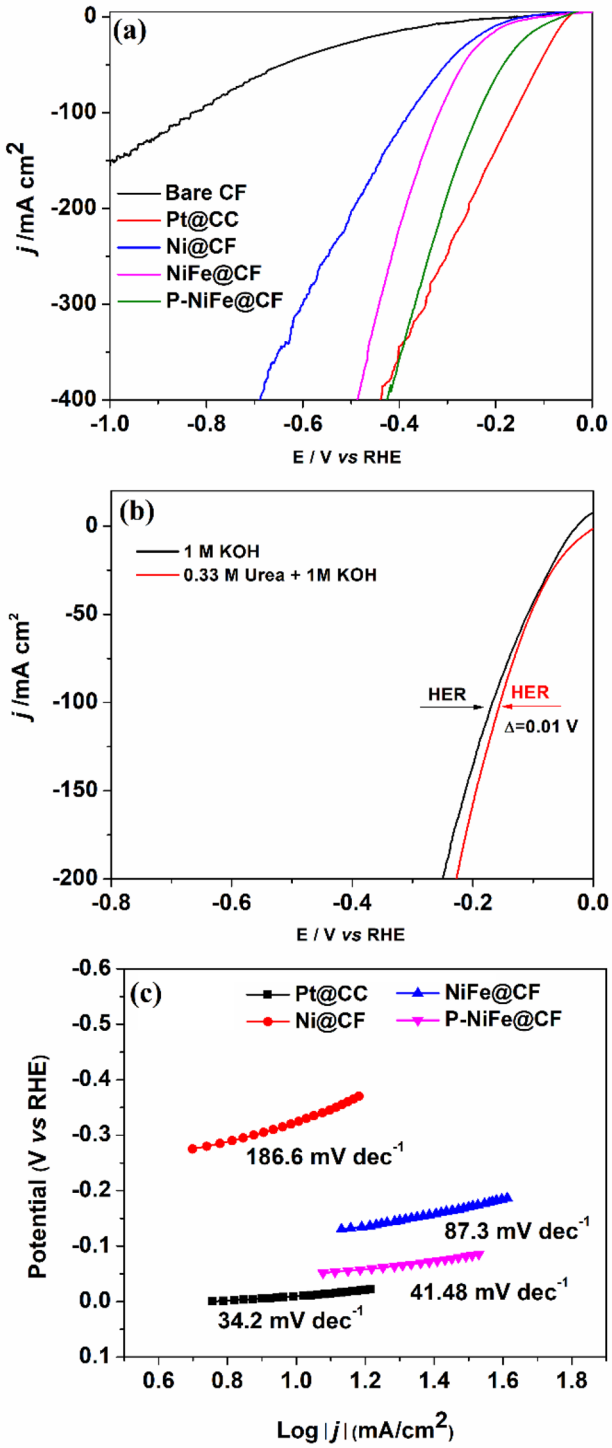

Figure 4. (**a**) LSV curves of different catalyst electrodes in 1.0 M KOH at a scan rate of 5 mV s^{-1}, (**b**) LSV curves of P-NiFe@CF in 1.0 M KOH with and without 0.33 M urea, and (**c**) Tafel plots of different catalysts in 1.0 M KOH.

NiOOH sites for water oxidation[54,55]. As shown in Fig. 3a, the electrode potential of P-NiFe@CF for the UOR decreased considerably to 1.39 V to attain a current density of 200 mA cm^{-2} compared to 1.59 V for the OER (i.e., water oxidation), which indicates the oxidation current increased considerably in the presence of urea, thus indicating that H_2 production by urea electrolysis was more energy efficient than water electrolysis. Figure 3a also shows the activities of the different catalysts for the UOR. Clearly, P-NiFe@CF required the lowest potential to attain a given current density for H_2 production, indicating its superior UOR activity. Importantly, the electrochemical activity of P-NiFe@CF for the UOR exceeds that reported in the literature (Table S1). Additionally,

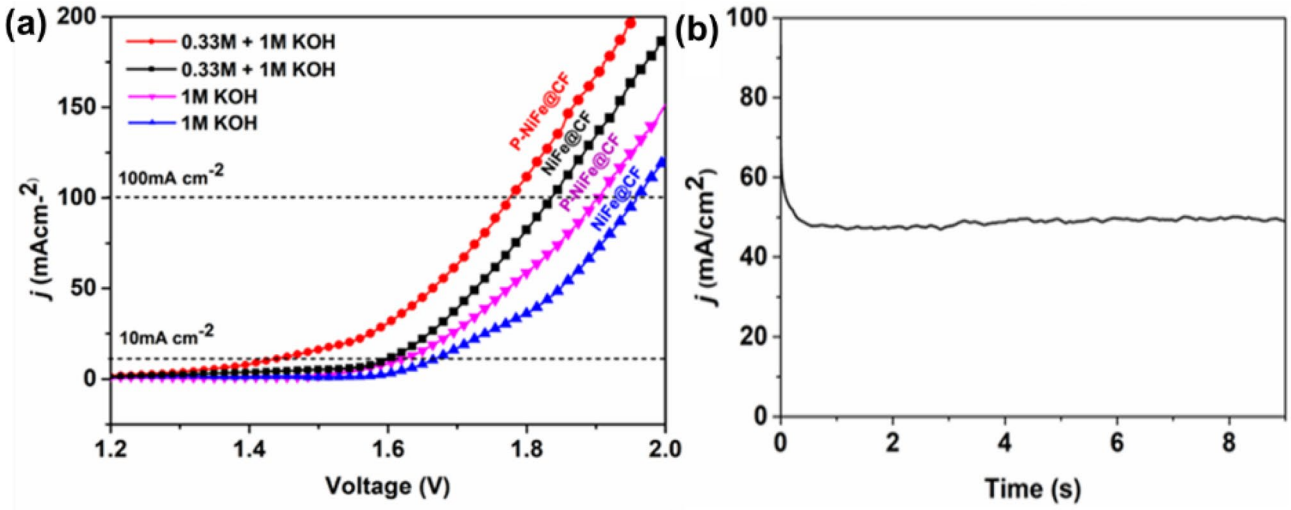

Figure 5. (**a**) Polarization curve of NiFe@CF and P-NiFe@CF in 1 M KOH with urea and without urea, and (**b**) a stability test in 1 M KOH and 0.33 M urea solution using P-NiFe@CF as anode and cathode at an applied potential corresponding to a current of 50 mA cm^{-2}.

the Tafel slope of P-NiFe@CF was 107.2 mV dec^{-1} which is much lower than those of Ni@CF and Ni–Fe@CF, as shown in Fig. 3b, further indicating faster kinetics of the UOR on P- NiFe@CF.

EIS measurements were conducted in a 1 M KOH solution to investigate the charge transfer rate (*Rct*) and double layer capacitance (C_{dl}), as shown in Fig. 3c. The EIS spectra were fitted with an equivalent circuit, as shown in the inset of Suppl. Fig. S4. The P-NiFe@CF electrode exhibited a significantly reduced R_{ct} compared to Ni–Fe@CF and Ni@CF, indicating considerably enhanced charge transfer kinetics of the UOR on the P-NiFe@CF catalyst[56,57]. The smaller R_{ct} value of P-NiFe@CF was possibly due to the improved conductivity of metallic bonds such as Ni_5P_4, NiP_2, and FeP, as the main factor. Furthermore, P-NiFe@CF featured the highest C_{dl} value, which was determined from the constant phase element value of the equivalent circuit (Suppl. Fig. S4), suggesting that P-NiFe@CF the highest electrochemically active surface area of the P-NiFe@CF[58]. This might be due to the higher valence state of Ni at the surface of P-NiFe@CF, as evidenced by the XPS analysis. Intimate contacts among the different crystal phases (Ni_5P_4, NiP_2, and FeP) might also affect the electronic structure, making it more favorable for the UOR as previously reported based on empirical and computational approaches[59,60]. Additionally, the electrochemical stability of Ni–Fe–P@CF was higher than that of Ni@CF and Ni–Fe@CF (Suppl. Fig. S4), plausibly owing to the formation of the metallic phosphide-rich surface of P-NiFe@CF, which could resist structural collapse during the Ni^{2+} to Ni^{3+} transition[61].

The HER performance of P-NiFe@CF was also analyzed by LSV in KOH with and without urea to examine its bifunctional catalytic activity for the UOR and HER. For comparative purposes, the HER activity of bare CF, Pt@CC, Ni@CF, and NiFe@CF was also studied for their HER performances, where the activity was indicated by the potential of the catalysts to achieve a given current density[2,4,62]. As evident from Fig. 4a, bare CF was inactive for the HER, with a negligible current density. The potential required for the Ni@CF electrode to attain 10 mA cm^{-2} was lowered from 0.124 to 0.104 V by Fe doping, and further considerably lowered to 65 mV by phospidation; however, it is still high than that (25 mV) of commercial Pt@CC. Additionally, P-NiFe@CF catalyst electrode had the highest stability among the evaluated catalysts (Suppl. Fig. S5). Interestingly, upon adding 0.33 M urea, a negative shift of only 10 mV was observed at a current density of 100 mA cm^{-2} (Fig. 4b), indicating that urea had little impact on the electrocatalytic activity for the HER. Figure 4c illustrates the Tafel plots of Pt@CC, P-NiFe@CF, NiFe@CF, and Ni@CF for the HER; demonstrating that P-NiFe@CF had a considerably lower Tafel slope of 41.4 mV dec^{-1} than NiFe@CF and Ni@CF, which is comparable with that (34.2 mV dec^{-1}) of Pt@CC.

Two electrode urea electrolysis cells were constructed using the bifunctional catalyst electrodes as both the anode and cathode. As seen in Fig. 5a, the urea electrolyzer with P-NiFe@CF electrodes featured a current density of 10 mA cm^{-2} at a cell voltage of 1.37 V, which is lower than that (1.61 V) of the cell with Ni–Fe@CF. Furthermore, a current of 100 mA cm^{-2} in the urea electrolyzer with P-NiFe@CF electrodes was achieved at a low cell voltage of 1.72 V, which exceeds those reported for Ni_3N/NF[63], Ni_3N NA/CC[64], Ni_2P/CC[65], MoS_2/Ni_3S_2[66], $Fe_{11.1\%}$-Ni_3S_2/NF[31], and Mo-NiP_2[67], as summarized in Suppl. Table S2. The P-NiFe@CF-based urea electrolyzer also exhibited good long-term electrochemical stability, as the current density remained stable for 8 h of operation at an applied voltage of 1.65 V after the initial drop due to concentration polarization[61] (Fig. 5b).

Conclusions

Bimetallic NiFe phosphides coated on CF by electroplating were successfully demonstrated to be efficient, free-standing, and bifunctional catalyst electrodes for the UOR and HER. P-NiFe@CF comprised Ni_5P_4, NiP_2, and FeP crystal phases, forming metallic bonds and partially oxidized surface Ni. The bifunctional electrocatalytic activity of the Ni-based catalyst for the UOR and HER was improved by Fe doping, and was further considerably enhanced by phosphodation, where the activity is outstanding compared to the literature reports. The electrolysis

cell with P-NiFe@CF as both the anode and cathode required only 1.42 V (*vs.* RHE) to attain a current density of 10 mA cm^{-2}, with good electrochemical stability. The results indicate that urea electrolysis is an energy-efficient method for hydrogen production as compared to water splitting, and bimetallic NiFe phosphides coated on CF can be used as an efficient free-standing bifunctional catalyst for the UOR and HER in urea electrolysis.

Data availability

The datasets generated during and/or analysed during the current study are available from the corresponding author on reasonable request.

Received: 26 August 2021; Accepted: 22 October 2021
Published online: 09 November 2021

References

1. Suryanto, B. H. R., Wang, Y., Hocking, R. K., Adamson, W. & Zhao, C. Overall electrochemical splitting of water at the heterogeneous interface of nickel and iron oxide. *Nat. Commun.* **10**, 5599 (2019).
2. Sayed, E. T. *et al.* Direct urea fuel cells: Challenges and opportunities. *J. Power Sources* **417**, 159–175 (2019).
3. Lan, R., Tao, S. & Irvine, J. T. S. A direct urea fuel cell: Power from fertiliser and waste. *Energy Environ. Sci.* **3**, 438–441 (2010).
4. Rollinson, A. N., Jones, J., Dupont, V. & Twigg, M. V. Urea as a hydrogen carrier: A perspective on its potential for safe, sustainable and long-term energy supply. *Energy Environ. Sci.* **4**, 1216–1224 (2011).
5. Kumar, G. G., Farithkhan, A. & Manthiram, A. Direct urea fuel cells: Recent progress and critical challenges of urea oxidation electrocatalysis. *Adv. Energy Sustain. Res.* **1**, 2000015 (2020).
6. Sun, X. & Ding, R. Recent progress with electrocatalysts for urea electrolysis in alkaline media for energy-saving hydrogen production. *Catal. Sci. Technol.* **6**, 1567–1581 (2020).
7. Yan, W., Wang, D. & Botte, G. G. Electrochemical decomposition of urea with Ni-based catalysts. *Appl. Catal. B* **127**, 221–226 (2012).
8. Hu, X., Zhu, J., Li, J. & Wu, Q. Urea electrooxidation: Current development and understanding of Ni-based catalysts. *ChemElectroChem* **15**, 3211–3228 (2020).
9. Singh, R. K., Rajavelu, K., Montag, M. & Schechter, A. Advances in catalytic electrooxidation of urea: A review. *Energy Technol.* **9**, 2100017 (2021).
10. Singh, R. K. & Schechter, A. Electrochemical investigation of urea oxidation reaction on β $Ni(OH)_2$ and $Ni/Ni(OH)_2$ Author links open overlay panel. *Electrochim. Acta* **278**, 405–411 (2018).
11. Zhu, B., Zibin, L. & Zou, R. Designing advanced catalysts for energy conversion based on urea oxidation reaction. *Small* **16**, 1906133 (2020).
12. Sun, X. & Ding, R. Recent progress with electrocatalysts for urea electrolysis in alkaline media for energy-saving hydrogen production. *Catal. Sci. Technol.* **10**, 1567–1581 (2020).
13. Singh, R. K., Subramanian, P. & Schechter, A. Enhanced urea activity of oxidation on nickel-deposited tin dendrites. *Chem. Electro. Chem.* **4**, 1037–1043 (2017).
14. Yu, Z. Y. *et al.* Ni-Mo-O nanorod-derived composite catalysts for efficient alkaline water-to-hydrogen conversion: Via urea electrolysis. *Energy Environ. Sci.* **11**, 1890–1897 (2018).
15. Sun, C. B., Guo, M. W., Siwal, S. S. & Zhang, Q. B. Efficient hydrogen production via urea electrolysis with cobalt doped nickel hydroxide-riched hybrid films: Cobalt doping effect and mechanism aspect. *J. Catal.* **381**, 454–461 (2020).
16. Hu, C. *et al.* In situ electrochemical production of ultrathin nickel nanosheets for hydrogen evolution electrocatalysis. *Chem* **3**, 122–133 (2017).
17. Liu, M., Jiao, Y., Zhan, S. & Wang, H. Ni_3S_2 nanowires supported on Ni foam as efficient bifunctional electrocatalyst for urea-assisted electrolytic hydrogen production. *Catal. Today* **355**, 596–601 (2019).
18. Babar, P. *et al.* Bifunctional 2D electrocatalysts of transition metal hydroxide nanosheet arrays for water splitting and urea electrolysis. *ACS Sustain. Chem. Eng.* **7**, 10035–10043 (2019).
19. Forslund, R. P. *et al.* Nanostructured LaNiO3 perovskite electrocatalyst for enhanced urea oxidation. *ACS Catal.* **6**, 5044–5051 (2016).
20. Park, S. W., Kim, I., Oh, S. I., Kim, J. C. & Kim, D. W. Carbon-encapsulated NiFe nanoparticles as a bifunctional electrocatalyst for high-efficiency overall water splitting. *J. Catal.* **366**, 266–274 (2018).
21. Liang, C. *et al.* Exceptional performance of hierarchical Ni-Fe oxyhydroxide@NiFe alloy nanowire array electrocatalysts for large current density water splitting. *Energy Environ. Sci.* **13**, 86–95 (2020).
22. Kumar, A. & Bhattacharyya, S. Porous NiFe-Oxide nanocubes as bifunctional electrocatalysts for efficient water-splitting. *ACS Appl. Mater. Interfaces* **9**, 41906–41915 (2017).
23. Młynarek, G., Paszkiewicz, M. & Radniecka, A. The effect of ferric ions on the behaviour of a nickelous hydroxide electrode. *J. Appl. Electrochem.* **14**, 145–149 (1984).
24. Wang, Z. *et al.* Coupling molecularly ultrathin sheets of NiFe-layered double hydroxide on $NiCo_2O_4$ nanowire arrays for highly efficient overall water-splitting activity. *ACS Appl. Mater. Interfaces* **9**, 1488–1495 (2017).
25. Wang, L. *et al.* Nitrogen-doped porous carbon/Co3O4 nanocomposites as anode materials for lithium-ion batteries. *ACS Appl. Mater. Interfaces* **6**, 7117–7125 (2014).
26. Wang, J., Ji, L., Zuo, S. & Chen, Z. Hierarchically structured 3D integrated electrodes by galvanic replacement reaction for highly efficient water splitting. *Adv. Energy Mater.* **7**, 1700107 (2017).
27. Zhu, D. *et al.* Two-dimensional metal–organic frameworks with high oxidation states for efficient electrocatalytic urea oxidation. *Chem. Commun.* **53**, 10906–10909 (2017).
28. Huo, J. *et al.* Bifunctional iron nickel phosphide nanocatalysts supported on porous carbon for highly efficient overall water splitting. *Sustain. Mater. Technol.* **22**, 1–9 (2019).
29. Chen, Q. *et al.* Bifunctional Iron-Nickel Nitride nanoparticles as flexible and robust electrode for overall water splitting. *Electrochim. Acta* **247**, 666–673 (2017).
30. Zhang, B. *et al.* Iron-nickel nitride nanostructures in situ grown on surface-redox-etching nickel foam: Efficient and ultrasustainable electrocatalysts for overall water splitting. *Chem. Mater.* **28**, 6934–6941 (2016).
31. Zhu, W. *et al.* Wet-chemistry topotactic synthesis of bimetallic iron-nickel sulfide nanoarrays: An advanced and versatile catalyst for energy efficient overall water and urea electrolysis. *J. Mater. Chem. A* **6**, 4346–4353 (2018).
32. Dutta, S., Indra, A., Feng, Y., Song, T. & Paik, U. Self-supported nickel iron layered double hydroxide-nickel selenide electrocatalyst for superior water splitting activity. *ACS Appl. Mater. Interfaces* **9**, 33766–33774 (2017).
33. Du, H., Kong, R. M., Guo, X., Qu, F. & Li, J. Recent progress in transition metal phosphides with enhanced electrocatalysis for hydrogen evolution. *Nanoscale* **10**, 21617–21624 (2018).

34. Xiao, X. *et al.* Electronic modulation of transition metal phosphide: Via doping as efficient and pH-universal electrocatalysts for hydrogen evolution reaction. *Chem. Sci.* **9**, 1970–1975 (2018).
35. Lammel, P. *et al.* Analysis of rain erosion resistance of electroplated nickel-tungsten alloy coatings. *Surf. Coat. Technol.* **206**, 2545–2551 (2012).
36. Liang, H. *et al.* Plasma-Assisted synthesis of NiCoP for efficient overall water splitting. *Nano Lett.* **16**, 7718–7725 (2016).
37. Zhang, Y. *et al.* A Mn-doped Ni2P nanosheet array: An efficient and durable hydrogen evolution reaction electrocatalyst in alkaline media. *Chem. Commun.* **53**, 11048–11051 (2017).
38. Hou, Y. *et al.* Ag@CoxP core-shell heterogeneous nanoparticles as efficient oxygen evolution reaction catalysts. *ACS Catal.* **7**, 7038–7042 (2017).
39. Liu, K. *et al.* High-performance transition metal phosphide alloy catalyst for oxygen evolution reaction. *ACS Nano* **12**, 158–167 (2018).
40. Tan, Y. *et al.* Versatile nanoporous bimetallic phosphides towards electrochemical water splitting. *Energy Environ. Sci.* **9**, 2257–2261 (2016).
41. Zhang, L., Chang, C., Hsu, C. W., Chang, C. W. & Lu, S. Y. Hollow nanocubes composed of well-dispersed mixed metal-rich phosphides in N-doped carbon as highly efficient and durable electrocatalysts for the oxygen evolution reaction at high current densities. *J. Mater. Chem. A* **5**, 19656–19663 (2017).
42. Hao, J., Yang, W., Zhang, Z. & Tang, J. Metal-organic frameworks derived CoxFe1-xP nanocubes for electrochemical hydrogen evolution. *Nanoscale* **7**, 11055–11062 (2015).
43. Li, Y. *et al.* Ternary NiCoP nanosheet arrays: An excellent bifunctional catalyst for alkaline overall water splitting. *Nano Res.* **9**, 2251–2259 (2016).
44. Nai, J., Lu, Y., Yu, L., Wang, X. & Lou, X. W. D. Formation of Ni–Fe mixed diselenide nanocages as a superior oxygen evolution electrocatalyst. *Adv. Mater.* **29**, 1–8 (2017).
45. Xuan, C. *et al.* Porous structured Ni-Fe-P nanocubes derived from a prussian blue analogue as an electrocatalyst for efficient overall water splitting. *ACS Appl. Mater. Interfaces* **9**, 26134–26142 (2017).
46. Ding, R. *et al.* Mesoporous Ni-P nanocatalysts for alkaline urea electrooxidation. *Electrochim. Acta* **222**, 455–462 (2016).
47. Zhang, X. *et al.* Vapour-phase hydrothermal synthesis of Ni2P nanocrystallines on carbon fiber cloth for high-efficiency H2 production and simultaneous urea decomposition. *Electrochim. Acta* **254**, 44–49 (2017).
48. Cao, K. *et al.* Ultra-high capacity lithium-ion batteries with hierarchical CoO nanowire clusters as binder free electrodes. *Adv. Funct. Mater.* **25**, 1082–1089 (2015).
49. Jin, T., Han, Q. & Jiao, L. Binder-free electrodes for advanced sodium-ion batteries. *Adv. Mater.* **32**, 1–14 (2020).
50. Ye, K. *et al.* Three-dimensional carbon- and binder-free nickel nanowire arrays as a high-performance and low-cost anode for direct hydrogen peroxide fuel cell. *J. Power Sources* **300**, 147–156 (2015).
51. Chen, S. *et al.* Stainless steel mesh supported nitrogen-doped carbon nanofibers for binder-free cathode in microbial fuel cells. *Biosens. Bioelectron.* **34**, 282–285 (2012).
52. Moosavifard, S. E., Fani, S. & Rahmanian, M. Hierarchical CuCo2S4 hollow nanoneedle arrays as novel binder-free electrodes for high-performance asymmetric supercapacitors. *Chem. Commun.* **52**, 4517–4520 (2016).
53. Xu, X., Tian, X., Zhong, Z., Kang, L. & Yao, J. In-situ growth of iron/nickel phosphides hybrid on nickel foam as bifunctional electrocatalyst for overall water splitting. *J. Power Sources* **424**, 42–51 (2019).
54. Liu, Y. *et al.* Facilely constructing 3D porous NiCo2S4 nanonetworks for high-performance supercapacitors. *New J. Chem.* **38**, 4045–4048 (2014).
55. Das, G., Tesfaye, R. M., Won, Y. & Yoon, H. H. NiO-Fe2O3 based graphene aerogel as urea electrooxidation catalyst. *Electrochim. Acta* **237**, 171–176 (2017).
56. Kwong, W. L., Lee, C. C. & Messinger, J. Scalable two-step synthesis of nickel-iron phosphide electrodes for stable and efficient electrocatalytic hydrogen evolution. *J. Phys. Chem. C* **121**, 284–292 (2017).
57. Liu, D. *et al.* High-performance urea electrolysis towards less energy-intensive electrochemical hydrogen production using a bifunctional catalyst electrode. *J. Mater. Chem. A* **5**, 3208–3213 (2017).
58. Yang, D., Yang, L., Zhong, L., Yu, X. & Feng, L. Urea electro-oxidation efficiently catalyzed by nickel-molybdenum oxide nanorods. *Electrochim. Acta* **295**, 524–531 (2019).
59. Li, P. & Zeng, H. C. Bimetallic Ni-Fe phosphide nanocomposites with a controlled architecture and composition enabling highly efficient electrochemical water oxidation. *J. Mater. Chem. A* **6**, 2231–2238 (2018).
60. Liu, P. F. *et al.* Ni2P(O)/Fe2P(O) interface can boost oxygen evolution electrocatalysis. *ACS Energy Lett.* **2**, 2257–2263 (2017).
61. Callejas, J. F., Read, C. G., Roske, C. W., Lewis, N. S. & Schaak, R. E. Synthesis, characterization, and properties of metal phosphide catalysts for the hydrogen-evolution reaction. *Chem. Mater.* **28**, 6017–6044 (2016).
62. Xu, W. *et al.* Highly active Ni-Fe double hydroxides as anode catalysts for electrooxidation of urea. *New J. Chem.* **41**, 4190–4196 (2017).
63. Hu, S. *et al.* Ni3N/NF as Bifunctional catalysts for both hydrogen generation and urea decomposition. *ACS Appl. Mater. Interfaces* **11**, 13168–13175 (2019).
64. Liu, Q. *et al.* A porous Ni3N nanosheet array as a high-performance non-noble-metal catalyst for urea-assisted electrochemical hydrogen production. *Inorg. Chem. Front.* **4**, 1120–1124 (2017).
65. Chen, S., Duan, J., Vasileff, A. & Qiao, S. Z. Size fractionation of two-dimensional sub-nanometer thin manganese dioxide crystals towards superior urea electrocatalytic conversion. *Angew. Chem. Int. Ed.* **55**, 3804–3808 (2016).
66. Li, F. *et al.* Heteroporous MoS2/Ni3S2 towards superior electrocatalytic overall urea splitting. *Chem. Commun.* **54**, 5181–5184 (2018).
67. Zhang, K., Zhang, G., Qu, J. & Liu, H. Intensification of anodic charge transfer by contaminant degradation for efficient H_2 production. *J. Mater. Chem. A* **6**, 10297–10303 (2018).

Acknowledgements

This work was supported by the Korea Institute of Energy Technology Evaluation and Planning (KETEP) grant funded by the Korea government (MOTIE) (20194030202290 and 2021400000690).

Author contributions

W.H.Y. carried out the experiments. G.D. designed the experimental work and wrote the manuscript. B.K. performed XRD and SEM analysis. B.J.P. designed the experimental work. H.H.Y. reviewed the manuscript. Y.S.Y. directed the research.

Competing interests

The authors declare no competing interests.

Additional information

Supplementary Information The online version contains supplementary material available at https://doi.org/10.1038/s41598-021-01383-3.

Correspondence and requests for materials should be addressed to H.H.Y. or Y.S.Y.

Reprints and permissions information is available at www.nature.com/reprints.

Publisher's note Springer Nature remains neutral with regard to jurisdictional claims in published maps and institutional affiliations.